Hindawi
Scientific Programming
Volume 2022, Article ID 3070361, 9 pages
https://doi.org/10.1155/2022/3070361

Research Article

Deep Learning-Based MR Imaging for Analysis of Relation between Cerebrospinal Fluid Variation and Communicating Hydrocephalus after Decompressive Craniectomy for Craniocerebral Injury

Yangming Mao,[1] **Zhouming Shen**,[1] **Jun Wang**,[2] **Haifeng Zhu**,[1] **Zhengyong Yu**,[1] **Xiang Chen**,[1] **and Hua Cheng**[1]

[1]*Department of Neurosurgery, Funing People's Hospital, Yancheng 224400, Jiangsu, China*
[2]*Department of Imaging, Funing People's Hospital, Yancheng 224400, Jiangsu, China*

Correspondence should be addressed to Hua Cheng; tianyixc@163.com

Received 29 July 2021; Revised 9 February 2022; Accepted 23 February 2022; Published 15 April 2022

Academic Editor: Gustavo Ramirez

The aim of this study was to analyze the relationship between cerebrospinal fluid variation and hydrocephalus through deep learning-based (DL-based) magnetic resonance imaging (MRI), in order to improve the postoperative recovery of craniocerebral injury (CI) patients and reduce the deterioration after decompressive craniectomy of the patient. 50 patients with CI who received the diagnosis and treatment at the hospital were chosen as the subjects. The retrospective analysis on patients with CI was conducted herein. First, the general clinical data of the patients were analyzed. Next, the MRI images for brain damage of the patients were collected. After that, the DL-based brain image classification and the artificial intelligence technology were utilized to solve the classification problems with classifiers. Finally, the DL-based convolutional neural network (CNN) was adopted to preprocess the image features, and the offline training and online reconstruction were conducted after the construction of the model. Four groups of databases were selected for deep learning and analyzed in terms of data feature analysis, principal component analysis (PCA), and application of 3D scale-invariant feature transformation (SIFT) operators in image data analysis. The results manifested that, the WHGO descriptor and the area under the curve were the largest. SIFI, PCA, and WHGO had the sensitivity of 87.5%, 88.2%, and 90.1%, the specificity of 91.8%, 90.1%, and 94.2%, and the correct rate of 90.6%, 87.5%, and 92.4%, respectively. The volume content of the cerebrospinal fluid in the subarachnoid space was 77.04% higher than that of cerebrospinal fluid in the ventricle. In conclusion, the intelligent deep learning model proposed in this article was able to assume the measurement of clinical cases and auxiliary diagnosis. This model not only can help doctors save the diagnosis time and enhance the medical efficiency, but also can precisely identify the patient's lesion area. Therefore, it had substantial application potential in mobile-based clinical practice.

1. Introduction

Craniocerebral damage is a common disease in neurosurgery. If the patient does not receive effective treatment, the cerebrospinal fluid varies with the intracranial pressure, resulting in an increase in the disability rate and mortality rate of the patient [1]. The cerebrospinal fluid flows through the lymphatic system by means of decreasing neurons and enters the perivascular space and the subarachnoid space [2] through the ependymal space. The hydrocephalus is composed of enhanced intracranial pressure, increased cerebrospinal fluid, and an enlarged ventricular system. In the early stage, the increased cerebrospinal fluid or malabsorption led to the accumulation of cerebrospinal fluid, an increase in intracranial pressure, and eventually the expansion of the subarachnoid space [3]. The communicating

hydrocephalus refers to the obstructions in the cerebrospinal fluid circulation which are located outside the ventricular system, the subarachnoid space, or the end point of cerebrospinal fluid absorption, and it is the disorder of arachnoid granules, which refers to the cerebrospinal fluid arising from the brain trauma, hemorrhage of cerebrovascular disease, intracranial infection, and postoperative hydrocephalus caused by subarachnoid adhesions. The classic classification method for hydrocephalus exerted a significant role in the selection of clinical treatment plans. Currently, the risk factors for extracranial hydrocephalus have not been comprehensively and systematically investigated. The decompressive craniectomy for severe craniocerebral injury has turned into the first treatment plan for severe craniocerebral injury, and it has also been extensively applied in clinical treatment. The factors for postoperative cerebrospinal fluid variation and the formation of communicating hydrocephalus have yet to be resolved.

Magnetic resonance imaging (MRI) can offer abundant information about anatomy and function and is equipped with lots of powerful functions. It has no ionizing radiation effects and can perform the computed tomography scan in any orientation including relaxation, unlike computed tomography technology. The MRI has many advantages such as proton density, chemical shift, high resolution, and high contrast ratio for soft tissue. Therefore, it is one of the most advanced diagnostic techniques in medical imaging diagnosis [4, 5]. The algorithms are introduced in the diagnosis for a disease of the MRI which can automatically complete lesion detection and data annotation, provide physicians with assistance in the diagnosis, and highly raise the efficiency of treatment [6]. The rapid MR scanning technology, hardware-paralleled imaging technology, and signal processing and data imaging method have all been applied in some commercial scanners. As a critical technology in accelerated magnetic resonance scanning, the imaging technology can make full use of coil sensitivity and combine with gradient encoding, to reduce the amount of data obtained in the reconstruction of magnetic resonance images and shorten the imaging time. The manifold topology and low iteration have accomplished great success in reconstruction under high-speed acceleration conditions. However, the artifacts in images hinder physicians' progress in diagnosing the lesion characteristics of the patient.

As artificial intelligence (AI) is being applied in computers, deep learning has been extensively used in organ segmentation and lesion detection in CT images [7]. The deep learning methods cover the target detection network, image segmentation network, and classification network. The target detection network completes the detection work using Faster RCNN, SSD, and so on; the segmentation network completes the detection relying on the U-Net-series methods and 3D convolution, and the classification network VGG is used to conduct the image segmentation to judge whether lesions exist or not [8]. No matter the DL-based image segmentation method for organs and lesions, or the DL-algorithm-based target detection method for lesions, has dramatically raised the diagnosis efficiency of disease in applications [9]. Therefore, the DL-based image lesion analysis has great significance in improving diagnosis efficiency and early treatment.

A great amount of accumulative medical imaging data offered a guarantee for the training and learning of AI. The deep learning of big data has proceeded through the reasonable system design and optimization of parameters [10]. DL becomes popular rapidly with the powerful computing capacity of graphic processing unit (GPU) and attracts extensive attention in signal processing and its multiple fields. In the field of image processing, it can realize quantifiable, real-time, and motion-insensitive magnetic resonance parameter imaging. DL-based MRI can improve the quality of medical images, accelerate image acquisition schemes, and improve the quality of output objects, which are conducive to the analysis by clinicians. The DL-based images assisted the physicians to make the diagnosis early, working out the active treatment plans and effective clinical decisions, by means of measuring, evaluating, classifying, diagnosing, and assisting preoperative design, so as to effectively facilitate the detection, recognition, and diagnosis of diseases using the medical imaging, and drive and realize the computer-assisted treatment in the medical and health field [11, 12]. Hence, CI patients were selected as the research objects, MRIs of brain injury were collected, an optimized DL model was constructed, and the lesion areas in images were recognized to lay a solid foundation for intelligent and autonomous assessment and classification. Besides, CI MRI was diagnosed. MRI helped doctors make decisions timely, formulate treatment schemes, and improve prognosis by early diagnosis to provide the support for clinical diagnosis and treatment.

2. Methods

2.1. Subjects. In this study, 50 patients with CI who received the diagnosis and treatment at the hospital from June 2018 to June 2020 were chosen as the subjects. The age of patients ranged from 38 to 65 years and the average age was 45.562 ± 2.74 years. The admission time lasted for 1–14 days. The initial symptoms include headaches, fever, convulsions, mental disorders, memory deterioration, and comprehension decline. The gender ratio and average age of the patients were compared, in which the difference had no statistical significance ($P > 0.05$). The experiment obtained approval from the ethics committee of the hospital, and all the patients and their family members have already known and signed the informed consent form.

Inclusion standard was as follows: (1) the patients whose frontal angle for lateral ventricle was 33%; 2) the patients whose penumbra around the ventricle had imaging characteristics and accompanied with obvious infection symptoms, such as fever, headache, general malaise, and other acute or subacute characteristics; (3) the patients whose bone window had ipsilateral, contralateral, and bilateral subdural effusion or interhemispheric effusion; and (4) the patients whose EEG showed focal abnormalities.

Exclusion standard was as follows: (1) the patients who had tumors in the central nervous system, intracranial hemorrhage, leukodystrophy, toxic encephalopathy, or

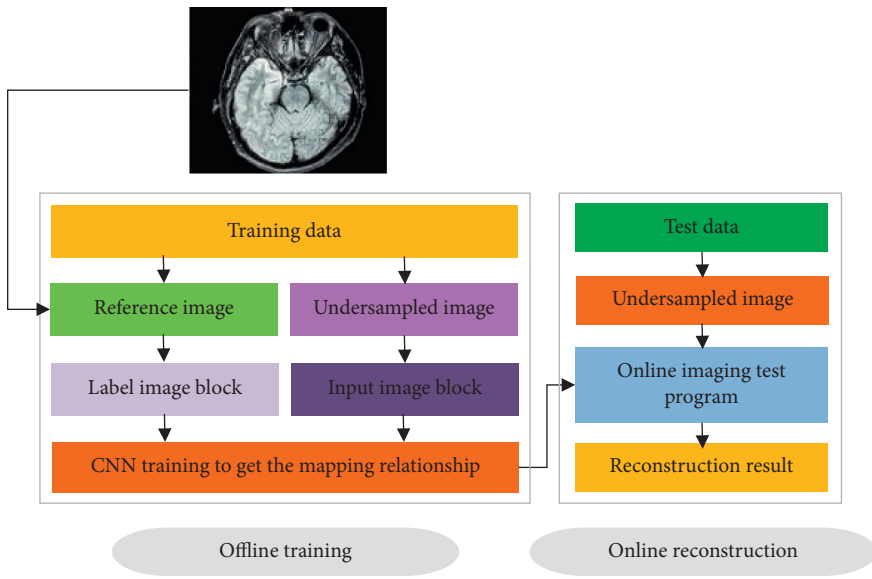

Figure 1: Flow diagram for fast MR imaging of deep learning.

metabolic brain diseases; (2) the old patients who were physically weak, suffered from severe cardiopulmonary liver and kidney dysfunction, and could not receive anesthesia; (3) MRI indicated that the patients got tumors, space-occupying lesions, aqueduct stenosis, and other confirmed obstructive hydrocephalus; and (4) the patients who suffered from brain atrophy, bilateral or unilateral ventricle enlargement, localized ventricle enlargement, and extracerebral hydrops.

2.2. Dynamic Contrast-Enhanced MR Scanning. In this study, MR 3.0 magnetic resonance instrument was adopted in the examination for the patients. It was required to describe the detailed examination procedures to the patient before scanning. Let the patient keep a supine gesture and maintain steady breathing. The earplugs were used to reduce the impact of equipment noise. The scanning sequence included the conventional MR and sagittal 3DT1WI. The scanning parameters for conventional MR sequence were shown as follows: axial T1WI sequence, matrix of 251×251, a layer thickness of 3.5 mm, a field of view of 25×25 cm, tilt angle of 15°, interlayer spacing of 6.1 mm, while the scanning parameters for the sagittal MR sequence were shown as follows: matrix of 256×256, a layer thickness of 1 mm, a field of view of 25×25 cm, a tilt angle of 8°, and no interval. The obtained magnetic resonance images were transmitted to the workstation and processed using the Functool II software.

The SPACE sequence of the MR instrument was used to distinguish the surrounding tissues from the cerebrospinal fluid in the T2WI image. The total volume of the cerebrospinal fluid was obtained by summing up all layers of the network, and the VR 3D image of the total cerebrospinal fluid was obtained. The ventricle cerebrospinal fluid was identified using the 2D growth click method, and the total volume of the ventricle cerebrospinal fluid was calculated.

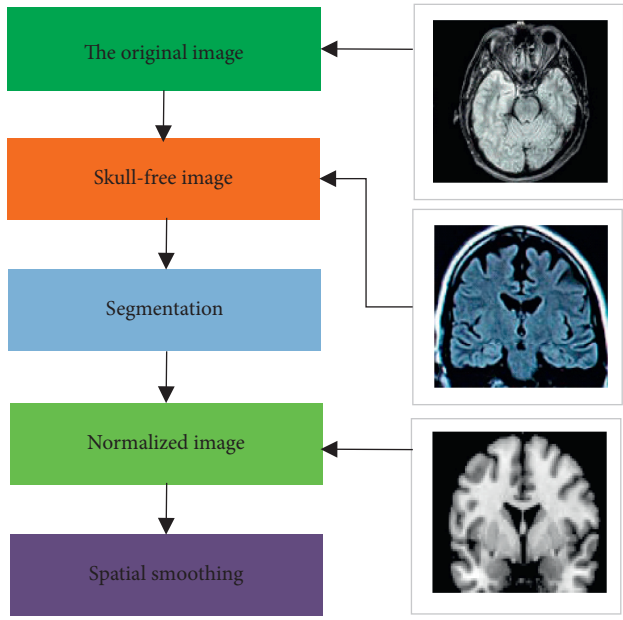

Figure 2: Flow diagram for preprocessing of MRI data.

2.3. Application of Deep Learning in Fast MR Imaging. The application of deep learning in MR imaging includes offline training and online reconstruction, with its general structure shown in Figure 1. First, the data collected through the MR scanning which is the data in fully sampled K-space can be regarded as training data. The training data is composed of the reference image and undersampled image, among which the former one is the label image block, while the latter one is the input image block. After training, the MRI system is used to collect new data, and then the undersampled images undergo an online reconstruction test. The training data and test data experience the convolutional neural network and obtain the mapping relationship between the input and the label, which indicates that the

parameter model is well trained, and the test data is reconstructed based on the model.

2.4. Flow Diagram for Preprocessing of MRI Data. In this study, all MRI data is preprocessed using SPM8 software and VBM8 toolkit and should be mapped to the standardized Montreal Neurological Association space. The standardized images are segmented into images for white matter, gray matter, and cerebrospinal fluid. The standardized and segmented images go through the quality inspection and smooth processing to obtain the target data. The specific image preprocessing procedure is shown in Figure 2. First, the original image is processed to obtain a skull-free head portrait, segmented to get a standardized image, and underwent a series of treatments of the system. The images with smoother space are obtained after noise reduction and artifact removal.

2.5. CNN-Based MR Images for Structure Model. The reconstructed convolutional neural network for MR images is mainly composed of the input layer, convolutional layer, activation layer, and output layer. There are 3 convolutional layers. Each convolutional layer is made up of multiple feature surfaces which are composed of multiple neurons. Each neuron is connected to the local area of the feature surface in the previous layer via the defined convolution kernel. The undersampled and multichannel image block is used as the network input. All fully sampled images pass through the square root of the sum-of-squares (SOS) to obtain a single-channel fully sampled image, which can be used as the output label of the network (Figure 3).

2.6. Feature Extraction. The schematic diagram for feature extraction is shown in Figure 4. When extracting features of image data, the information on the local area is obtained using dense sampling, and the local area is described through the network for feature extraction, to get the feature matrix of the subject. The data codebook is constructed using the algorithm adopted in the network. The feature frequency in the codebook represents the spatial subblock. The feature channel training classifier is used later.

2.7. Construction of CNN Model. The convolutional neural network is composed of the input layer, convolutional layer, undersampled layer, and output layer. The convolutional layer consists of several computing layers. Each computing layer has multiple feature mappings, of which each represents a defined plane. The neurons in the same plane have identical weights. The specific convolutional equation is shown as follows:

$$X_j^k = g\left(\sum_{i\in N_j} X_i^{k-1} * l_{ij}^k + a_i^k\right). \tag{1}$$

In (1), N_j represents the local receptive area of the neuron j, X_i^{k-1} indicates the output value of the neuron i in $k-1$ layer, l_{ij}^k stands for the No. j weight of the neuron i, and a_i^k represents the biased number of i in No. k layer. The undersampled layer refers to the feature extraction layer. Provided that m feature images are processed by the undersampled layer, the number of images is not changed, and the size of images is obviously smaller. The specific calculation equation is shown as follows:

$$X_j^k = g\left(\delta^k \mathrm{dec}\left(z_i^{k-1}\right) + a^k\right). \tag{2}$$

In (2), dec() represents the undersampling, δ^k indicates the adjustment parameter, which is a constant, and a^k stands for an adjusting bias. The full connection layer is intimately connected to the previous layer. The sigmoid function is adopted to calculate the full-connection layer. The specific method is shown as follows:

$$X_j^k = g\left(\sum_{i\in N_j} v_{ji} * X_i^{k-1} + a^k\right). \tag{3}$$

In (3), v_{ji} represents the weight between No. i input and No. j output in No. $k-1$. a^k indicates the trainable bias. The type of samples in the output layer is determined by the samples in the input layer. The maximum probability of samples in the input layer corresponds to the final type of output samples. The stochastic gradient descent is adopted in the training of the algorithm. The basic calculation equation is shown as follows:

$$\lambda_j := \lambda_j - \phi \frac{\partial}{\partial \lambda_j} J(\lambda). \tag{4}$$

In (4), ϕ indicates learning efficiency, and the step size of gradient descent can be adjusted. The extremely small ϕ value will reduce the converging speed of the algorithm, and the extremely big value will hinder the normal converge of the algorithms. ϕ is 0.2 in the algorithm of the study. The Gaussian mixture model is adopted in the optimized processing. Provided that the random variable X is subjected to the Gaussian distribution $M(\eta, \sigma^2)$, the probability density function of the Gaussian function is expressed as follows:

$$g(x) = \frac{1}{\sqrt{2\pi}\sigma} \exp\left(-\frac{(x-\eta)^2}{2\sigma^2}\right). \tag{5}$$

In (5), η represents the mathematical expectation and σ^2 indicates the variance. The probability density function of the Gaussian mixture model is expressed as follows:

$$Q(x_i|\psi) = \sum_{l=1}^{L} \pi_l Q_l(x_i|\phi_l). \tag{6}$$

In (6), π_l indicates the coefficient of the density function of the Gaussian mixture model, which is the No. l weighted value in the Gaussian distribution. Ψ represents the parameter vector in the mixture model, ϕ_l indicates the Gaussian distribution parameter, and Q_l represents the probability density function in the No. l Gaussian mixture distribution. The parameter value can be estimated according to the maximum density function. The following

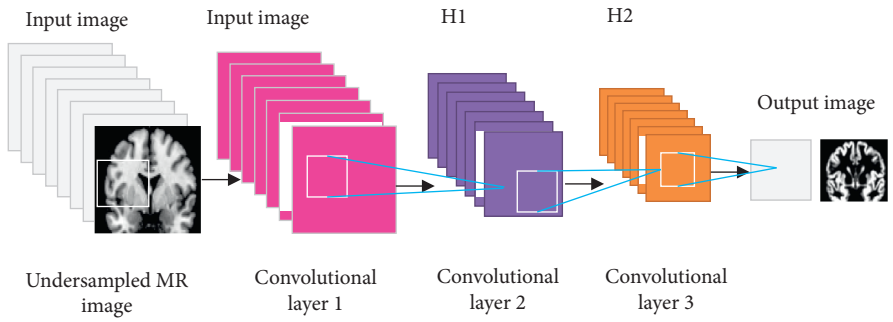

Figure 3: Diagrams for training structure of CNN-based MR reconstruction model.

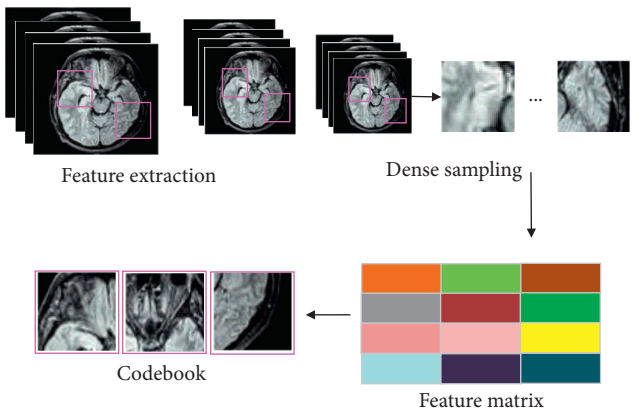

Figure 4: Schematic diagram for feature extraction.

estimation equations are generally adopted in the calculation:

$$Q(X \mid \psi) = \Pi_{i=1}^{M} Q(x_i \mid \psi) = K(\psi \mid X), \quad \psi = \arg\max L(\psi \mid X). \tag{7}$$

In general, the partial derivative of some variables is used to obtain the maximum value of the function, and the parameters are modified and iterated to converge the maximum error range.

When learning a model, the classifier can be regarded as a task, to find the relationship between features and categories in a training set. If the classifier is able to predict the category of the new sample, the relationship between the features and the category of the classifier can be easily confirmed. When evaluating the accuracy of the category in the test set, a subject will be reserved as a test set. $n-1$ indicates the training set for subjects, TC indicates the accurate number predicted by male subjects, while TB represents the accurate number predicted by female subjects. If the male subjects are predicted as the number of female subjects, it will be denoted by FV. If the female subjects are predicted as the number of male subjects, it will be expressed by FS.

The equation for sensitivity (SS) is shown as follows:

$$\mathrm{SS} = \frac{TC}{TC + FV}. \tag{8}$$

The equation for specificity (SC) is shown as follows:

$$\mathrm{SC} = \frac{TB}{TB + FS}. \tag{9}$$

The accuracy also is a feature of the quantized classifier, and the calculation equation is shown as follows:

$$GR = \frac{TC + TB}{TC + FV + TB + FS}. \tag{10}$$

[0, 1] represents the range of the above three evaluation indicators. If the calculation result is closer to 1, it means the segmentation effect is more ideal. The sensitivity refers to the ratio of accurate prediction of male subjects, while the specificity refers to the ratio of accurate prediction of female subjects. The generalization rate refers to a sum of accuracies of all subjects.

2.8. Statistical Method. The SPSS21.0 software was used in the statistical processing of experimental data. The measurement data which conformed to the normal distribution was indicated by the mean value ± standard deviation ($\bar{x} \pm s$), whereas measurement data that did not conform to the normal distribution was represented by the frequency and frequency (%). $\alpha = 0.05$ served as the test standard for group comparison. The continuous variable was expressed as mean ± standard deviation. The comparison of deviations was verified by independent sample t and chi-square test. $P < 0.05$ indicated that the difference had statistical significance.

3. Results

3.1. MRI Images. Magnetic resonance imaging (MRI) means that, under the assistance of the external magnetic field, the protons were rotating around the magnetic field to increase the precession angle in the action of radiofrequency waves. The signal was converted into an image after being processed through the computer network. Figure 5 shows the MRI images for the brains of different patients.

3.2. Acquisition of Image Data. The MR scanning data were selected from the open database for healthy adults. The feasibility of the test system was achieved through network training. The information on the subjects is shown in Table 1.

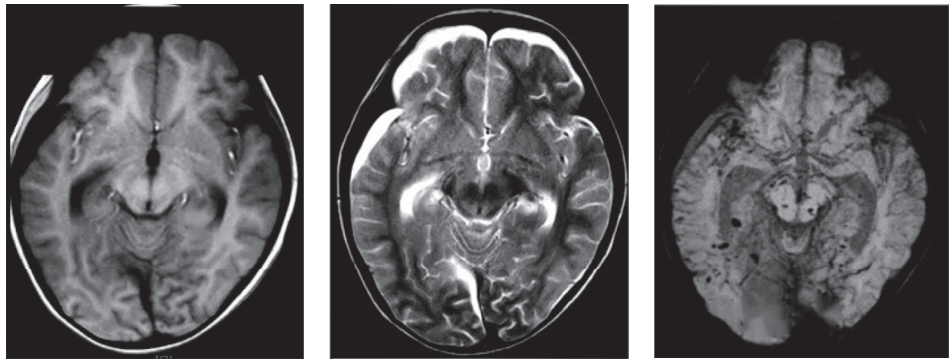

(a) (b) (c)

Figure 5: MRI images for craniocerebral injury. (a) T1WI; (b) T2WI; (c) SWI.

Table 1: Information on subjects in 3 centers.

Data set		Female	Male	Total
A	Number	80	83	163
	Age	23.6 ± 2.1	22.5 ± 1.81	20.4 ± 1.9
	Age range	18–24	18–27	18–26
B	Number	102	62	164
	Age	22.8 ± 2.31	20.4 ± 1.81	21.6 ± 2.32
	Age range	19–31	19–30	19–31
C	Number	50	42	92
	Age	45.6 ± 20.3	47.8 ± 22.16	43.7 ± 18.81
	Age range	18–72	18–65	18–69
D	Number	41	46	87
	Age	44.7 ± 19.8	46.2 ± 14.2	45.7 ± 18.61
	Age range	19–80	19–72	19–75

Table 1 shows that the information about subjects was selected from three centers (A, B, and C). 163 subjects were selected from center A, including 80 female patients and 83 male patients; 164 subjects were chosen from center B, including 102 female patients and 62 male patients; 92 subjects were selected from center C, including 50 female patients and 42 male patients; and 87 subjects were chosen from center D, including 41 female patients and 46 male patients.

3.3. ROC Curve in Data Set. The PCA method is a kind of complicated model to identify gender differences in brain structures. The SIFI operator was applied in the test of MRI data and had an elaborate description in the neuroimaging scanning area of the individual structure. The characteristics of four groups of subjects in Table 1 were analyzed in terms of receiver operating characteristic (ROC), principal component analysis (PCA), and 3-dimensional scale-invariant feature transform (3D SIFT). The SIFI operator was applied in the analysis of other image data. Figure 6 shows the comparison of the ROC curve of the WHGO descriptor mentioned in the article. The higher WHGO descriptor and the area under the curve (AUC) manifested that method we proposed achieved a certain result in the identification of gender, and the model classifier had better classification performance.

3.4. Measurement Method. The sensitivity, specificity, and correct rate of data sets in group A were compared by means of three methods, as shown in Figure 7. The data evaluation indicators in group A showed that the correct rate of WHGO is apparently higher than those of SIFI and PCA. The sensitivity of SIFI, PCA, and WHGO was 87.5%, 88.2%, and 90.1%, the specificity was 91.8%, 90.1%, and 94.2%, and the correct rate was 90.6%, 87.5%, and 92.4%.

3.5. Relations between Imaging Features and Hydrocephalus. The interhemispheric hydrocephalus was closely related to hydrocephalus after decompressive craniectomy for craniocerebral injury. The relationship between imaging features and hydrocephalus was analyzed after 50 craniocerebral injury patients underwent the decompressed operation and treatment, as shown in Figure 8. Figure 8(a) displays 22 patients who got postoperative hydrocephalus and 28 patients who had noncomplicated hydrocephalus. Figure 8(b) shows 11 patients who had hydrocephalus complicated with poor prognosis, 8 patients who got noncomplicated hydrocephalus, 15 patients who had hernia in the bone window of the brain tissue, and 9 cases of hernia in the bone window without hydrocephalus.

3.6. Total Volume of Intracranial Cerebrospinal Fluid and Volume of Cerebrospinal Fluid of Communicating Hydrocephalus Patients. The hydrocephalus refers to a pathological state in which the cerebrospinal fluid is accumulated in the ventricular system or subarachnoid space due to the production, absorption, or circulation of cerebrospinal fluid. Figure 9 shows the distribution of the total volume of intracranial cerebrospinal fluid and the average volume of cerebrospinal fluid in the ventricle and subarachnoid space of communicating hydrocephalus patients. The total volume of cerebrospinal fluid was 445.2 cm^3, of which the difference was of statistical significance ($P < 0.05$), the ventricle cerebrospinal fluid was 157.2 cm^3, the subarachnoid cerebrospinal fluid was 278.3 cm^3, and the content of subarachnoid cerebrospinal fluid was 77.04% higher than that of the ventricular cerebrospinal fluid.

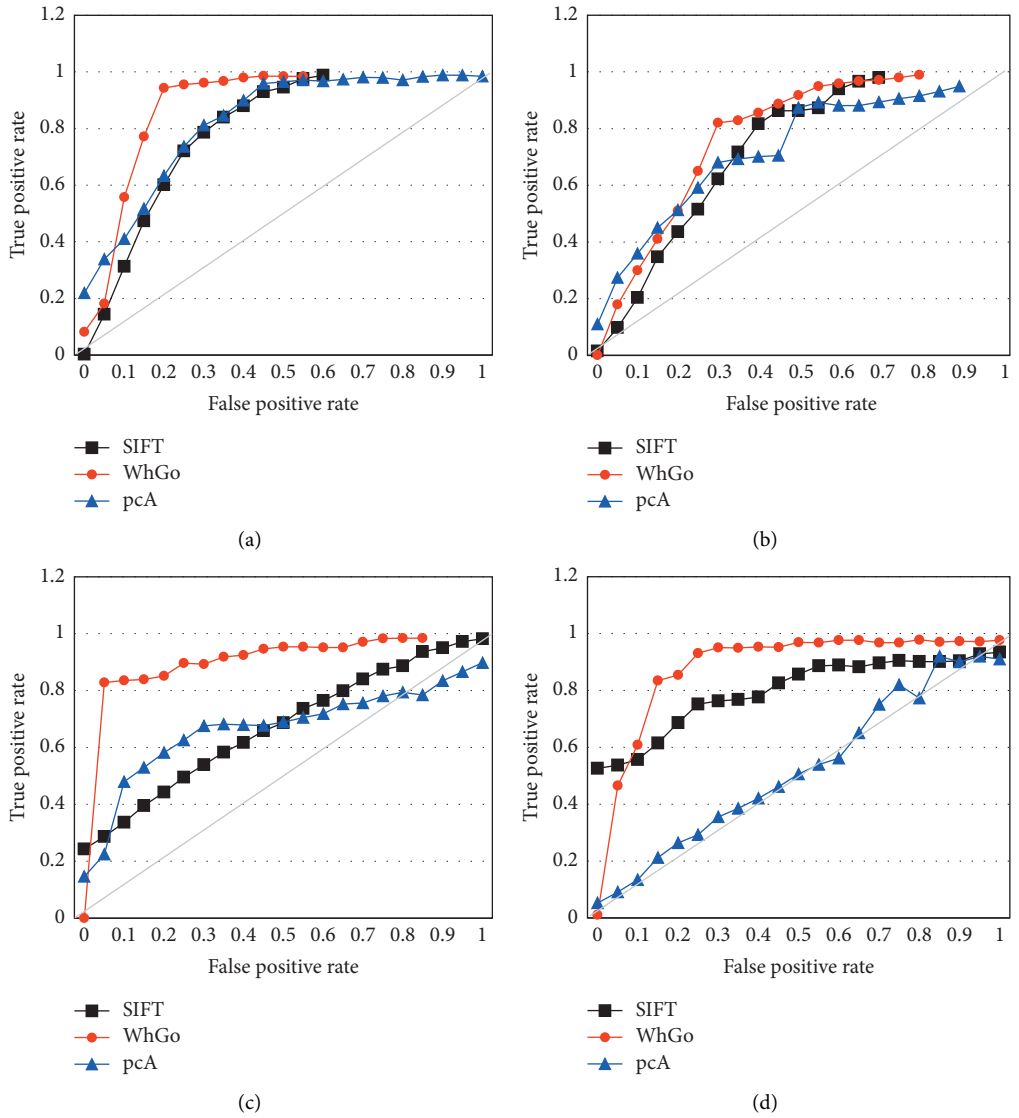

Figure 6: ROC curve of four types of data.

4. Discussion

The decompressive craniectomy can effectively treat craniocerebral injury patients and reduce intracranial pressure. The CI patients can be effectively treated through craniocerebral injury, which may damage the mechanism of pressure balance in the brain of the patient. A series of clinical symptoms and complications are emerged herein, involving CSF incision leakage, intracranial infection, subdural effusion, skull defect syndrome, and other problems [13]. The study conducted by Benjamini et al. [14] showed that multidimensional MRI might provide noninvasive biomarkers for the detection of brain injury. Among the patients with traumatic brain injury, multidimensional MRI biomarkers distinguish normally appearing white matter from mild and severe encephalopathy. After CI, the balance between the production and absorption of cerebrospinal fluid is affected. In addition, there were a series of changes in patients' imaging features. The included MRI could display

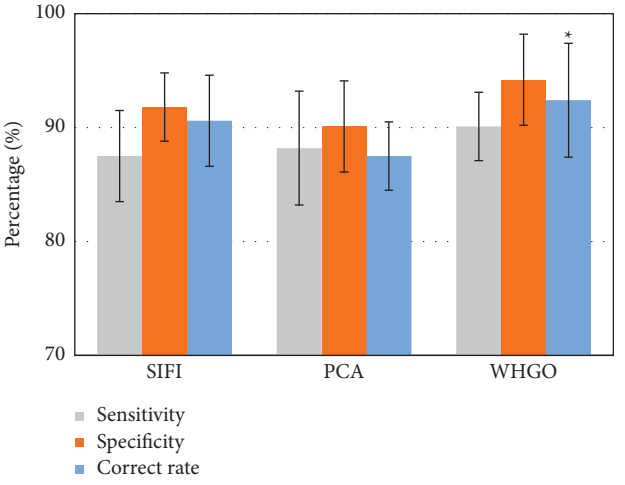

Figure 7: Comparison of evaluation indicators. * indicates the statistical differences, while $P < 0.05$ represents the statistical significance.

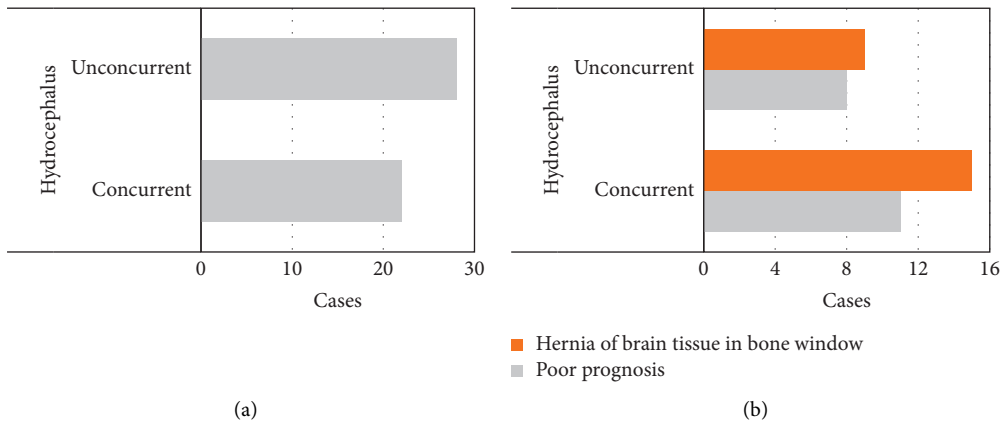

Figure 8: Relation between imaging features and hydrocephalus.

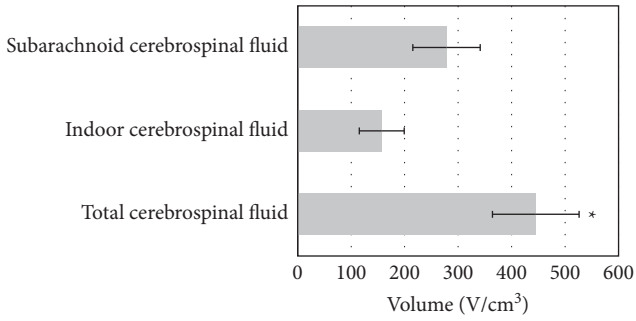

Figure 9: Volume and content of the cerebrospinal fluid. ∗ indicates that the differences show significant meaning, $P < 0.05$.

the images of hydrocephalus patients and noncomplicated hydrocephalus patients. The distribution of the total volume of intracranial cerebrospinal fluid and the average volume of cerebrospinal fluid in the ventricle and subarachnoid space of communicating hydrocephalus patients showed that the content of the cerebrospinal fluid in subarachnoid space was 77.04% higher than that in the ventricle.

In this category of systems, a majority of computers were equipped with DL-based algorithms and can summarize and conclude the features and rules based on a large number of medical images with expert labels the computer have learned and accumulated [15], and finally obtain an expert-level diagnosis level, which was widely applied in clinical practice. Hu et al. [16] used convolutional network segment brain MRI semantic images. The results indicated that the brain MRI segmentation model showed high accuracy and the intelligent algorithm had excellent robustness in the anatomic results of the segmentation of brain MRI. A convolutional network was utilized to extract the features of MRI of CI patients and it showed excellent effects. Kang et al. [17] used DL features and machine learning classifiers to classify brain tumors. The integration of DL helped improve the performance significantly, and the support vector machine (SVM) with the basis function kernel was superior to other machine learning classifiers. Besides, the receptors' features were analyzed and the WHGO descriptor showed that the model classifier had excellent classification performance.

For instance, some MRI-based AI pulmonary nodule screening systems achieved remarkable results in terms of fracture detection, evaluation of bone fragility, and child's bone age [18]. Brito et al. [19] proposed that the convolutional neural networks were applied to extract features from images for the patient, to generate coordinates in the lesion area in the image and preselected detection framework. The suspicious parts were classified with a trainer. The slight adjustment of detection framework changed the shortcomings in features of the traditional manually designed detection object. The deep convolutional network has abundant features and can accurately detect the location of the lesion.

There are more and more trends for artificial intelligence and medical research, providing a new orientation for the studies on digital medical applications. The different AI models play a very important role in the treatment of bone injuries. The studies showed that the 3D feature description operator (3D WHGO) presented excellent identification ability and had a higher resolution for data. The integration of local information and global information can improve classification performance. It was reported in the literature that the differences were common in the human brain, in terms of gender, size, shape, and brain capacity, and were microscopic differences. The MRI data were different from natural long diameter images. The discriminativeness cannot be obtained in the mode recognition. It was believed in some studies that the volume of cerebrospinal fluid can be gained after the communicating hydrocephalus patients underwent MR sequence examination. The MRI was used in the research and analysis of cerebrospinal fluid. The arterial pressure did not decline and was transmitted farther, due to a drop in contraction of the arterial wall or subarachnoid space, resulting in the increase in pulse pressure in the brain and the expansion of the ventricular system [20]. In this article, DL-based magnetic resonance imaging was collected to study the relationship between cerebrospinal fluid and hydrocephalus in CI patients. The content of subarachnoid cerebrospinal fluid was 77.04% higher than that of ventricle cerebrospinal fluid. The progress of the hydrocephalus of the patients can be judged via MRI.

5. Conclusion

In this article, the DL-based algorithm MRI images detection was analyzed to raise the efficiency of the diagnosis of bone injuries. The study showed that the deep convolutional neural network is able to classify and sort up the MRI images. The CNN can collect data at a very fast speed and did not subject to the interference of surrounding tissues of hydrocephalus, so as to obtain the 3D images for hydrocephalus. The DL-based artificial intelligence model not only can save the diagnosis time for a doctor but also can raise the medical efficiency, which had a fundamental clinical significance. The study still has some disadvantages, for instance, deep learning needs to rely on a flood of data; however, the study has no adequate data and just possesses a high-precision model for central data. It is required to collect the data from different medical centers, to improve the stability of the system. Little subarachnoid hemorrhage can hardly be displayed in MRI. How to present little hemorrhage in intelligent programs is also a direction of future study.

Data Availability

The data used to support the findings of this study are available from the corresponding author upon request.

Conflicts of Interest

The authors declare no conflicts of interest.

References

[1] S. Schur, P. Martel, and J. Marcoux, "Optimal bone flap size for decompressive craniectomy for refractory increased intracranial pressure in traumatic brain injury: taking the patient's head size into account," *World Neurosurgery*, vol. 137, pp. e430–e436, 2020.

[2] P. Missori, C. Morselli, M. Domenicucci et al., "Measurement of bone flap surface area and midline shift to predict overall survival after decompressive craniectomy," *World Neurosurgery*, vol. 96, pp. 11–14, 2016.

[3] A. Morice, F. Kolb, A. Picard, N. Kadlub, and S. Puget, "Reconstruction of a large calvarial traumatic defect using a custom-made porous hydroxyapatite implant covered by a free latissimus dorsi muscle flap in an 11-year-old patient," *Journal of Neurosurgery: Pediatrics*, vol. 19, no. 1, pp. 51–55, 2017.

[4] S. Inokuchi, N. Fujita, H. Hasegawa et al., "[Frontal base penetrating brain injury by a gardening scissors:A case report]," *Noshinkeigeka*, vol. 46, no. 11, pp. 999–1005, 2018, Nov;.

[5] S. Pezeshk, "3D convolutional neural networks for automatic detection of pulmonary nodules in chest CT," *IEEE Journal of Biomedical & Health Informatics*, vol. 23, no. 5, pp. 2080–2090, 2018.

[6] P.-H. Tsai, Y.-C. Chen, S.-W. Chiang et al., "Changes in sensorimotor-related thalamic diffusion properties and cerebrospinal fluid hydrodynamics predict gait responses to tap test in idiopathic normal-pressure hydrocephalus," *European Radiology*, vol. 28, no. 11, pp. 4504–4513, 2018.

[7] X. Q. Lv, L. Wu, and Y. Gu, "Detection of low dose CT pulmonary nodules based on 3D convolution neural network," *Guangxue Jingmi Gongcheng/Optics and Precision Engineering*, vol. 26, no. 5, pp. 1211–1218, 2018.

[8] Y. Xiao, J. Wu, Z. Lin, and X. Zhao, "A deep learning-based multi-model ensemble method for cancer prediction," *Computer Methods and Programs in Biomedicine*, vol. 153, pp. 1–9, 2018.

[9] S. L. Al-Khafaji, J. Zhou, A. Zia, and A. W.-C. Liew, "Spectral-spatial scale invariant feature Transform for hyperspectral images," *IEEE Transactions on Image Processing*, vol. 27, no. 2, pp. 837–850, 2018.

[10] X. Shao, H. Zhang, Y. Wang et al., "Deep convolutional neural networks combine Raman spectral signature of serum for prostate cancer bone metastases screening," *Nanomedicine: Nanotechnology, Biology and Medicine*, vol. 29, Article ID 102245, 2020.

[11] Q. Guan, Y. Wang, B. Ping et al., "Deep convolutional neural network VGG-16 model for differential diagnosing of papillary thyroid carcinomas in cytological images: a pilot study," *Journal of Cancer*, vol. 10, no. 20, pp. 4876–4882, 2019.

[12] R. Q. Chen and S. M. Xie, "Lung tumor detection method based on deep learning," *Computer Technology and Development*, vol. 19, no. 4, 2018.

[13] M. Shioji, T. Yamamoto, T. Ibata, T. Tsuda, K. Adachi, and N. Yoshimura, "Artificial neural networks to predict future bone mineral density and bone loss rate in Japanese postmenopausal women," *BMC Research Notes*, vol. 10, no. 1, p. 590, 2017.

[14] D. Benjamini, D. Iacono, M. E. Komlosh, D. P. Perl, D. L. Brody, and P. J. Basser, "Diffuse axonal injury has a characteristic multidimensional MRI signature in the human brain," *Brain*, vol. 144, no. 3, pp. 800–816, 2021.

[15] E. Oh, S. W Seo, Y. C Yoon, D. W Kim, S Kwon, and S Yoon, "Prediction of pathologic femoral fractures in patients with lung cancer using machine learning algorithms: comparison of computed tomography-based radiological features with clinical features versus without clinical features," *Journal of Orthopaedic Surgery (Hong Kong)*, vol. 25, no. 2, Article ID 2309499017716243, 2017.

[16] Y. Hu, H. Zhao, W. Li, and J Li, "Semantic image segmentation of brain MRI with deep learning," *Zhong nan da xue xue bao. Yi xue ban = Journal of Central South University. Medical sciences*, vol. 46, no. 8, pp. 858–864, 2021.

[17] J. Kang, Z. Ullah, and J. Gwak, "MRI-based brain tumor classification using ensemble of deep features and machine learning classifiers," *Sensors*, vol. 21, no. 6, Article ID 2222, 2021.

[18] Y. Ding, J. H. Sohn, M. G. Kawczynski et al., "A deep learning model to predict a diagnosis of alzheimer disease by using 18F-fdg PET of the brain," *Radiology*, vol. 290, no. 2, pp. 456–464, 2019.

[19] C. Brito, A. Machado, and A. Sousa, "Electrocardiogram beat-classification based on a ResNet network," *Studies in Health Technology and Informatics*, vol. 264, pp. 55–59, 2019.

[20] J. Cai, F. Xing, A. Batra et al., "Texture analysis for muscular dystrophy classification in MRI with improved class Activation mapping," *Pattern Recognition*, vol. 86, pp. 368–375, 2019.